




# Toward efficient and industrially compatible fully textured perovskite silicon tandem solar cells: Controlled process parameters for reliable perovskite formation

Oussama Er-raji<sup>1,2</sup>  | Alexander J. Bett<sup>1</sup>  | Stefan Lange<sup>4</sup> | Henning Nagel<sup>1</sup> | Martin Bivour<sup>1</sup> | Oliver Schultz-Wittmann<sup>1</sup> | Christian Hagendorf<sup>4</sup> | Martin Hermle<sup>1</sup> | Juliane Borchert<sup>1,2</sup> | Stefan W. Glunz<sup>1,2,3</sup>  | Patricia S. C. Schulze<sup>1</sup>

<sup>1</sup>Fraunhofer Institute for Solar Energy Systems ISE, Freiburg, Germany

<sup>2</sup>Department of Sustainable Systems Engineering (INATECH), University of Freiburg, Freiburg, Germany

<sup>3</sup>Cluster of Excellence livMatS@FIT-Freiburg Center for Interactive Materials and Bioinspired Technologies, University Freiburg, Germany

<sup>4</sup>Fraunhofer Center for Silicon Photovoltaics CSP, Otto-Eißfeldt-Straße 12, Halle, Germany

## Correspondence

Oussama Er-raji, Fraunhofer Institute for Solar Energy Systems ISE, 79110 Freiburg, Germany.

Email: [oussama.er-raji@ise.fraunhofer.de](mailto:oussama.er-raji@ise.fraunhofer.de)

## Funding information

Fraunhofer LIGHTHOUSE PROJECT MaNITU; German Federal Ministry for Economic Affairs and Climate Action, Grant/Award Number: 03EE1086A

## Abstract

Capitalizing on the existing silicon industry, fully textured perovskite-silicon tandem solar cells have a great potential to penetrate the electricity market. While the use of textured silicon with large pyramid size ( $> 1 \mu\text{m}$ ) enhances the power conversion efficiency (*PCE*), it also presents process complications. To achieve high performance, meticulous control of deposition parameters on textured silicon is required. This study provides a guideline for the use of the hybrid evaporation/spin-coating route to form high-quality perovskite absorbers. Using various characterization techniques, we highlight intrinsic differences between perovskite growth on flat versus textured substrates. Furthermore, we provide pathways to ensure a high perovskite phase purity, reveal mitigation strategies to avoid the formation of undesired dendritic perovskite structures, give guidelines to ensure photostability, and discuss the “misleading” effect of residual  $\text{PbI}_2$  on the perovskite photoluminescence response. A good understanding of the perovskite growth on textured silicon enables the fabrication of a tandem device with a *PCE*  $> 26\%$  (without employing additives or surface treatments) and a good operational stability. The comprehensive guidelines in this study provide a better understanding of perovskite formation on textured silicon and can be transferred when upscaling the hybrid route perovskite deposition.

## KEYWORDS

fully textured, hybrid route, impact of textured silicon, perovskite silicon tandem solar cells, photovoltaics, wide bandgap perovskite

## 1 | INTRODUCTION

In less than 8 years of development, perovskite silicon tandem solar cells have taken the lead as the best-performing double-junction solar cell technology.<sup>1</sup> Among other factors, this achievement is

mainly due to optimizing the perovskite deposition via solution processing to uniformly coat textured-front silicon bottom solar cells with small pyramid heights  $< 1 \mu\text{m}$ .<sup>2–7</sup> Simulation studies predict a further enhancement in the power conversion efficiency (*PCE*) by adopting the fully textured tandem architecture.<sup>8–10</sup> That is the fabrication of

This is an open access article under the terms of the [Creative Commons Attribution-NonCommercial-NoDerivs](https://creativecommons.org/licenses/by-nc-nd/4.0/) License, which permits use and distribution in any medium, provided the original work is properly cited, the use is non-commercial and no modifications or adaptations are made.

© 2023 The Authors. Progress in Photovoltaics: Research and Applications published by John Wiley & Sons Ltd.

the perovskite sub-cell on a double-side textured silicon bottom cell with pyramid heights  $> 1 \mu\text{m}$ , representing the current standard in the silicon PV industry. In this architecture, the perovskite absorber conformally follows the silicon texture pattern instead of forming a very thick layer which renders the top surface flat. With that, the fully textured tandem cell is expected to have reduced reflection losses in the blue-rich part of the spectrum which raises the short-circuit density ( $j_{\text{sc}}$ ) of the device.<sup>11,12</sup> Moreover, taking into account module integration, it is expected to achieve the highest energy yield in the field.<sup>13,14</sup> Nevertheless, standard perovskite solution processing is incompatible with large pyramids as it leads to shunting problems (uncovered Si pyramids).<sup>15,16</sup>

To solve this issue, the hybrid evaporation/spin-coating route emerged as the state-of-the-art processing technique for conformal perovskite growth on textured silicon with large pyramid height.<sup>17</sup> It consists of the following three steps: 1) evaporation of inorganic perovskite precursors to form a porous scaffold, 2) wet-chemical deposition of organic perovskite precursors to infiltrate into the formed scaffold, and 3) annealing to initiate precursors interdiffusion and perovskite crystallization.<sup>18</sup> The hybrid route merges the benefits of both, the solution process and the vacuum-based deposition, giving high compositional flexibility without using reactive and toxic solvents.<sup>16</sup> It has been used to fabricate high-efficiency devices on small active areas ( $\sim 1 \text{ cm}^2$ ).<sup>17,19–25</sup> More recently the spin-coating step has been replaced by blade coating, spray coating, and inkjet printing, which demonstrates the scalability perspective of this processing route.<sup>20,26,27</sup>

One of the most important factors to achieve highest performance for fully textured perovskite silicon tandem solar cells is a well-controlled deposition of the perovskite film and ensuring high bulk and surface quality. This becomes more difficult on textured silicon due to the introduced surface roughness. To date, there is no comprehensive study that analyses the influence of process parameters on the film quality for perovskite absorbers deposited via the hybrid route on textured silicon with pyramid heights  $> 1 \mu\text{m}$ . In this work, we provide a practical guideline for the use of the hybrid evaporation/spin-coating route to form high-quality wide-bandgap perovskite absorbers. Using various characterization techniques, we highlight intrinsic differences between perovskite growth on flat versus textured substrates. Furthermore, the following aspects are addressed: 1) we provide pathways to efficiently tune the perovskite optical bandgap and shed light on the impact of cesium halides in the evaporation step; 2) we reveal the critical impact of the organohalide mixture on the perovskite layer uniformity and present mitigation strategies to avoid undesired dendritic perovskite film formation; 3) we provide multiple strategies to achieve a high perovskite phase purity based on the  $\text{A}^+$  site cation engineering scheme; 4) we investigate in-depth the impact of  $\text{PbI}_2$  phases which are common when using the hybrid route and discuss their effect on charge extraction as well as the “misleading” perovskite photoluminescence response; and 5) we analyze the impact of cesium content in the absorber and identify the optimal regime where perovskite photostability is ensured. A good understanding of the perovskite formation on textured silicon enables the

fabrication of a tandem device with a  $\text{PCE} > 26\%$  (without employing additives or surface treatments) and good operational stability.

## 2 | EXPERIMENTAL SECTION

### 2.1 | Solar cell fabrication

Perovskite single-junction solar cell fabrication: perovskite single-junction cells were fabricated according to the procedure in our previous publication.<sup>18</sup>

Perovskite silicon tandem solar cell fabrication: the perovskite top cell and the silicon bottom cell processing were similar to the procedure described in ref.<sup>28</sup> Information on process parameter variation is mentioned within the text.

### 2.2 | Characterization

UV-vis measurements: to derive absorptance curves, reflectance ( $R$ ), and transmittance ( $T$ ) measurements were conducted using a lambda 950 spectrometer (PerkinElmer). Measurements were carried out in the wavelength range of 250–1,200 nm with a 2 nm step size. Absorptance ( $A$ ) was calculated by the formula  $A = 1 - R - T$ . The Tauc method was applied to determine the optical bandgap.<sup>29</sup>

PL measurements: steady-state photoluminescence (PL) measurements were performed using the LuQY Pro instrument from Quantum Yield Berlin. A 532 nm laser was used to excite the perovskite absorber. The equivalent laser intensity was set to approximately 1 sun, the spot size to  $0.1 \text{ cm}^2$ , and the resolution time to 3 s.

SEM measurements: for cross-sectional and top-view scanning electron microscopy (SEM) images, a Schottky emission SEM model Auriga 60 (Zeiss) device was used. The acceleration voltage was set to 5 kV. Top-view measurements were taken with a  $45^\circ$  angle.

XRD: X-ray diffraction (XRD) measurements were carried out with a Bruker D8 Advance diffractometer in the Bragg–Brentano geometry. The tool was equipped with a Cu anode tube at 40 mA/40 kV. Measurements were performed in the  $2\theta$  range of  $5^\circ$ – $45^\circ$ , with a step size and time per step of  $0.03^\circ$  and 0.1 s, respectively. Data analysis was carried out with the DIFRAC.EVA software.

XPS: X-ray photoelectron spectroscopy (XPS) was performed using a Kratos Axis Ultra DLD photoelectron spectrometer with monochromatized  $\text{Al K}\alpha$  radiation at 1486.6 eV acting as excitation source. The anode was operated at a power level of 225 W. Survey spectra between 1,330 eV and  $-5 \text{ eV}$  were recorded with a pass energy of 80 eV, 0.5 eV step width, and 200 ms dwell time over a measurement area of  $300 \times 700 \mu\text{m}^2$ . The chemical composition of the sample surface was quantified using the instrument-specific library of relative sensitivity factors (RSF). Depth profiling was achieved by scanning a focused beam of Ar ions across the sample with 1 keV kinetic energy.

ToF-SIMS: time-of-flight secondary ion mass spectrometry (ToF-SIMS) was conducted with a TOF.SIMS VI from the company

IONTOF GmbH. A liquid-metal ion gun (LMIG) was used as the primary ion source, providing  $\text{Bi}^+$  ions at a kinetic energy of 30 keV. The source was operated in high current bunched mode, where the pulsed  $\text{Bi}^+$  current is about 1.5 pA. Depth profiles in negative secondary ion polarity were recorded using the  $\text{Cs}^+$  sputter source. The accelerating voltage was 1,000 eV, and the beam current was 85 nA. The measurement window was  $100 \mu\text{m} \times 100 \mu\text{m}$  in size, and the sputtering window was chosen to be  $300 \mu\text{m} \times 300 \mu\text{m}$  to avoid edge effects. An electron flood gun and the non-interlaced mode with 0.3 s pause between sputter and  $\text{Bi}^+$  beam provided sufficient charge compensation. A special sample holder for azimuthal rotation with a velocity of  $\sim 30$ – $60$  rpm was used to minimize depth profile broadening effects due to the surface texture in conjunction with shading effects originating from the geometric arrangement between primary and sputter beams.

**jV measurements:** for tandem solar cells, current–voltage (jV) measurements were carried out using a Wacom solar simulator equipped with two filtered light sources, a halogen lamp, and a xenon lamp. Prior to the measurement, the spectral response was measured for the cell. Lamp intensities were then calculated following the procedure described by Meusel et al.<sup>30</sup> and adjusted with the help of two filtered WPVS reference solar cells. After calibration, the device was kept in open-circuit conditions under illumination for 3 hours. jV curves were recorded using a Keithley 2400 source meter in forward then reverse direction (range from  $-0.1$  V to  $1.85$  V, scan speed  $34$  mV/s, step width  $20$  mV). Between the single measurement points of the jV curve, the solar cell is under open circuit condition. A shadow mask was used to limit light exposure area to the  $1 \text{ cm}^2$  cell active area. For single-junction solar cells, jV measurements were performed with a solar simulator equipped with a xenon short arc lamp and a Keithley 2651A source meter. Using a silicon reference cell, the light intensity was calibrated to 1 sun under AM1.5g spectrum. Spectral mismatch was not considered. The measurements were done in the forward scan, then in the reverse scan with a scan speed of  $34$  mV/s, a range of  $-0.1$  V to  $1.2$  V, and a voltage step of  $20$  mV. A shadow

mask was used to limit the exposure area to the individual  $0.25 \text{ cm}^2$  cell active area.

**EQE:** The external quantum efficiency was measured as described in our previous publication.<sup>31</sup> Note that the measured EQEs are not absolute. Details can be found in [10.1002/solr.202200948](https://doi.org/10.1002/solr.202200948).

### 3 | RESULTS AND DISCUSSION

In this work, we opt for a  $1.66$  eV wide bandgap perovskite absorber with the composition  $\text{FA}_x\text{Cs}_{1-x}\text{Pb}(\text{I}_y\text{Br}_{1-y})_3$ . While the introduction of methylammonium ( $\text{MA}^+$ ) in the A-site (of the  $\text{ABX}_3$  perovskite crystal structure) has been reported to enhance the perovskite bulk quality,<sup>32–34</sup> other reports emphasize avoiding  $\text{MA}^+$ , even in small amounts, as it compromises the absorber's thermal stability.<sup>35–38</sup> For the latter reason, a double cation double halide perovskite composition is pursued.

For a conformal perovskite deposition on textured silicon, the hybrid evaporation/spin-coating route is used. In the first step, inorganic compounds  $\text{CsX}$  ( $\text{X} = \text{Br}, \text{I}$ ) and  $\text{PbI}_2$  are co-evaporated to form a conformal inorganic scaffold (alternatively called a template) on the substrate. Subsequently, an organohalide mixture of  $\text{FABr/FAI}$  ( $\text{FA} = \text{formamidinium}$ ) dissolved in ethanol is spin-coated onto the scaffold. Finally, an annealing step in air at  $150^\circ\text{C}$  for 25 mins induces precursor interdiffusion and perovskite formation.<sup>18</sup> A sketch of the hybrid route as well as influencing process parameters can be seen in Figure 1.

#### 3.1 | Bandgap tuning and layer uniformity: influence of the organohalide mix

To achieve current-matching in a monolithic perovskite silicon tandem solar cell, the most employed strategy is optimization of the perovskite optical bandgap ( $E_g$ ) and thickness.<sup>31,39–45</sup> With the hybrid route,

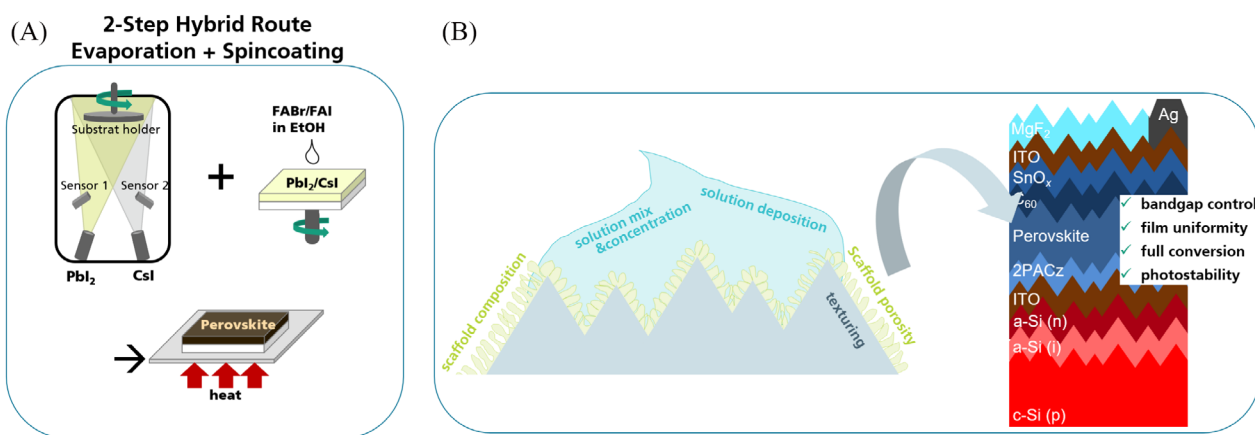


**FIGURE 1** Perovskite hybrid route processing and pathways to tune its properties. (A) The hybrid evaporation/spin-coating route for perovskite formation on micrometer-sized textured silicon (reprint with permission from author<sup>16</sup>) and (B) critical process parameters investigated in this work for the formation of a high-quality perovskite absorber.

the optical bandgap can be mainly tuned by varying the organohalide mixture (FABr/FAI) and to a lesser extent the CsX:PbI<sub>2</sub> evaporation rate ratio (Figure 2A). The displayed optical bandgaps in the graph are extracted by fitting the absorbance curves (from reflection and transmission measurements) via the Tauc method. Using the most reported inorganic scaffold in literature, CsBr:PbI<sub>2</sub> = 10%,<sup>17,19–21,23–25</sup> a wide range of optical bandgaps ranging from 1.55 eV with an FAI solution up to 1.76 eV with a FABr rich solution, can be achieved (Figure 2A). By mixing the organohalides, easy bandgap tuning is possible. The steady increase in  $E_g$  with higher FABr is due to the inclusion of bromide, which has a smaller radius in comparison to iodide, thereby reducing the perovskite crystal lattice and enlarging the bandgap.<sup>46,47</sup> If the commonly reported evaporation precursor CsBr is replaced with CsI, the optical bandgap is shifted downward due to higher iodide content in the perovskite composition. This allows reaching optical bandgaps down to 1.52 eV. Regarding the impact of the CsX:PbI<sub>2</sub> rate ratio, by increasing the Cs content, for a given solution mixture, the optical bandgap can be slightly increased. This is because a higher cesium cation incorporation induces octahedral tilting and reduces symmetry, which leads to bandgap widening.<sup>48–50</sup>

From Figure 2A, we determine that achieving the targeted 1.66 eV optical bandgap is possible by either combining a CsBr:PbI<sub>2</sub>

scaffold with an organohalide solution mix FABr/FAI = 50/50 or a CsI:PbI<sub>2</sub> template with an organohalide solution mix FABr/FAI = 65/35. Interestingly, Figure 2B shows that, for a similar bandgap (1.66 eV), the optical absorbance property of the perovskite absorber synthesized with CsBr as evaporation precursor is greater than that with CsI. The enhanced absorbance over the range between 250 nm and 747 nm is mainly attributed to a reduced reflectance. To understand whether this enhancement is due to a specific CsBr precursor property or is stemming from a distinct reaction with the organohalides, we evaluate the optical absorbance quality of all 54 perovskite compositions reported in Figure 2A.

Figure 3A–F displays the reflectance, transmittance, and absorbance curves of perovskite compositions synthesized with CsX:PbI<sub>2</sub> = 10% (X = I or Br) and a variation in organohalide mixture (the results of the other four variations CsX:PbI<sub>2</sub> = 12% and 15% can be found in Figure S1). Particularly, we find that using a FABr/FAI solution mixture ≤ 50/50 (labeled as critical regime in Figure 2A) induces a systematic reduction in the reflectance curve along the spectrum, which ultimately results in an enhanced optical absorbance. That is, independently of the co-evaporated cesium halide, the use of a solution mixture inside the critical regime leads to a systematic improvement of the absorbance. Consequently, the increased

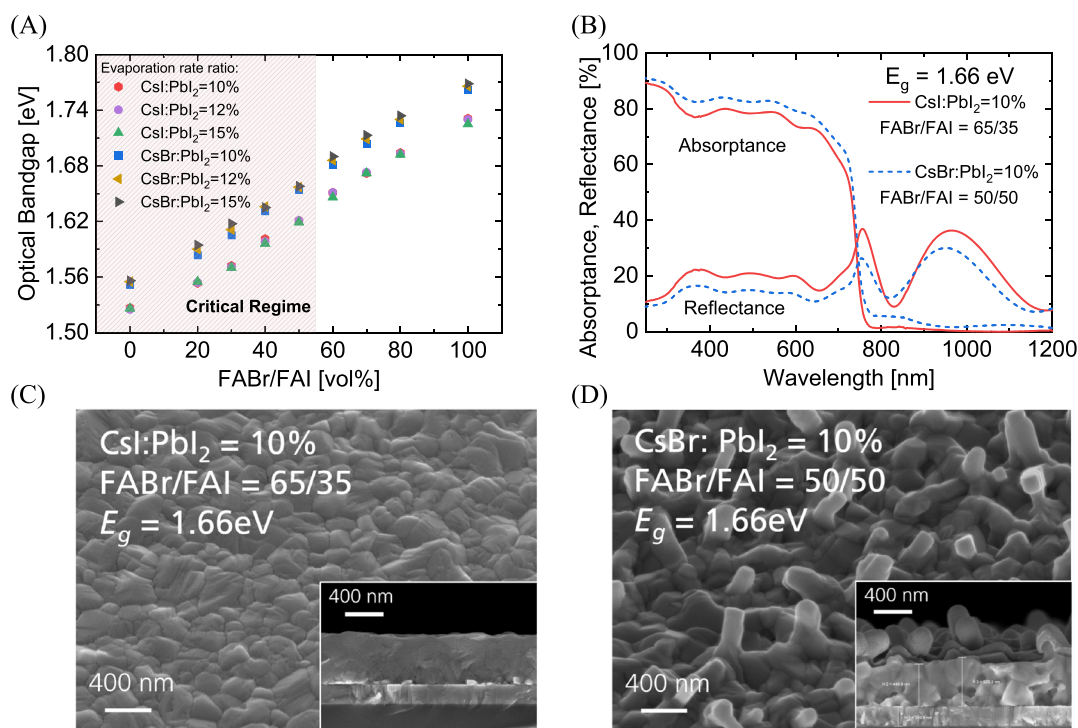


**FIGURE 2** Influence of the co-evaporation precursors and the organohalide solution mixture on the perovskite absorber's optical bandgap, absorbance property, and layer uniformity. (A) Optical bandgap (extracted via Tauc method) as a function of the organohalide mix (FABr/FAI with 0.45 M molarity) spin-coated on top of six different scaffolds with either CsI or CsBr as co-evaporation precursor with PbI<sub>2</sub> (CsX:PbI<sub>2</sub> = 10%, 12% or 15% rate ratio, X = I or Br). The targeted bandgap is 1.66 eV. The shaded area labeled “critical regime” designates the solution space which results in a dendritic perovskite film formation. The substrate is glass/perovskite, and the scaffold thickness is set to 300 nm. (B) Absorbance and reflectance spectra and (C,D) top-view and cross-section scanning electron microscopy (SEM) images of two perovskite absorbers synthesized with either CsI or CsBr as co-evaporation precursor with PbI<sub>2</sub> and their corresponding FAX solution mixture to achieve 1.66 eV optical bandgap.

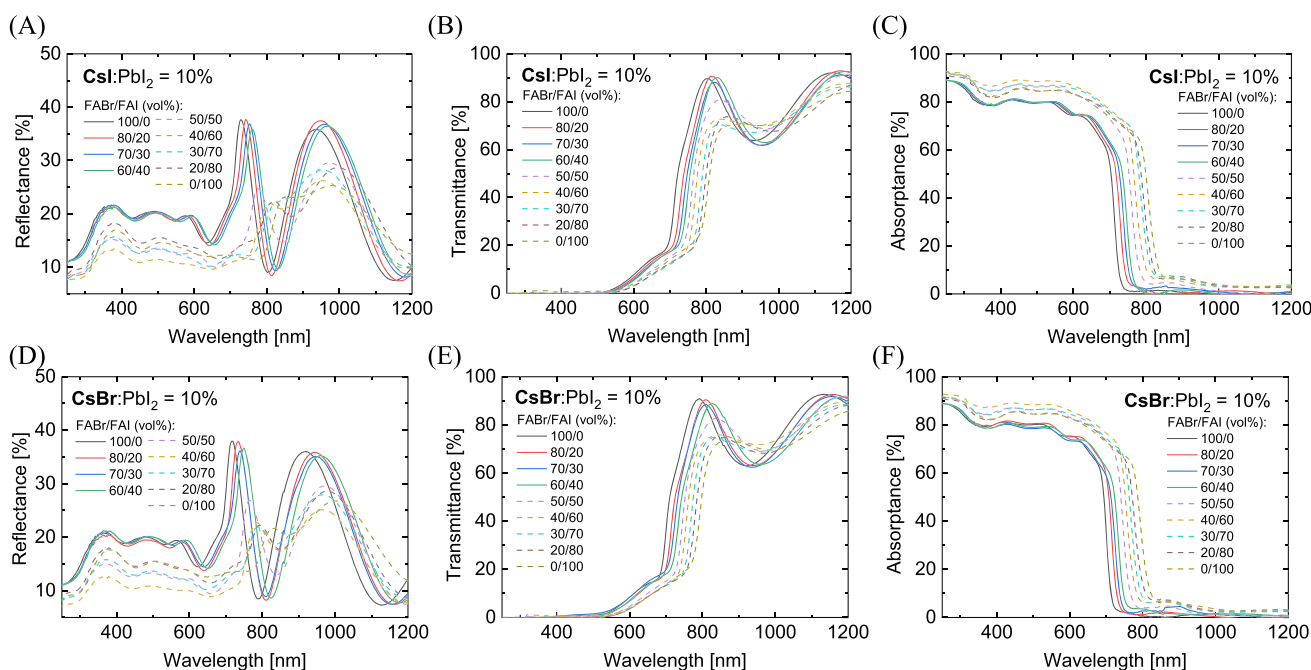


**FIGURE 3** Influence of the organohalide solution mixture on the perovskite absorber's optical bandgap, reflectance, transmittance, and absorbance properties. (A,B) Reflectance, (C,D) transmittance, and (E,F) absorbance curves of perovskite absorbers formed with either CsI or CsBr and  $\text{PbI}_2$  as co-evaporation precursors and a systematic variation in organohalide solution mixture (FABr/FAI = 100/0 to FABr/FAI = 0/100).

absorbance of the 1.66 eV perovskite absorber synthesized with CsBr in comparison to CsI is solely ascribed to the used solution mixture. Cross-sectional and top-view SEM images reveal a dendritic film formation with surface nanostructures in the perovskite synthesized with a solution mixture inside the critical regime (Figure 2C). On the other hand, a smooth and uniform surface is obtained outside the critical regime (Figure 2D). This observation is reproducible in different batches and is replicated on textured substrates as highlighted in Figure S2.

For all the perovskites in the critical regime, we assume that the dendrites/nanostructures on top of the perovskite surface, with a length ranging from 100 nm to > 800 nm, can interact with light (similar wavelength) and enhance the light incoupling, which reduces reflection and leads to a higher absorbance. While this property is appealing, the randomly distributed dendrites can also create shunt paths due to non-conformal formation of subsequent thin charge transport layers (CTLs), and therefore should be avoided. From a structural point of view, no additional phase could be detected in the X-ray diffractograms of the perovskite absorbers inside the critical regime (neither on flat nor on textured substrate) as can be seen in Figure S3. This indicates that the additional nanostructures have a perovskite crystal structure. Dendritic perovskite film formation has been previously reported in literature.<sup>51</sup> The driving force for dendrite growth requires some anisotropy,<sup>52</sup> usually of the interfacial energy between crystal and solution/liquid.<sup>51,53</sup> When mixing different organohalides (as performed in Figure 2A), a change in the difference in chemical potential that drives crystal growth will lead to a change

in the anisotropy. We suspect that once the iodide content in the solution equals or exceeds the bromide content (FABr/FAI  $\leq$  50/50, toward the critical regime), the crystal tends to grow in a more anisotropic direction, leading to a dendritic film formation. It thus becomes clear that for the hybrid route, tuning the organohalide mixture is not only necessary for optimizing the perovskite bandgap but also for ensuring a uniform layer formation, which is crucial to prevent non-conformal CTL and electrode coverage.

### 3.2 | Influence of the substrate on perovskite morphology and composition

Next to the organohalide mixture, the perovskite growth with the hybrid route is governed by the evaporated scaffold's morphology. Here, intrinsic differences arise for evaporated films on flat-front vs textured-front substrates (pyramid height > 1  $\mu\text{m}$ ). While the evaporated CsI/ $\text{PbI}_2$  scaffold presents a dense and compact film formation on a flat substrate, the layer appears porous on textured silicon (Figure 4A–D). The high porosity of the inorganic template is a desired attribute, since it enables a better infiltration of the organohalide solution in the second wet-chemical step, and thereby to the formation of a homogeneous perovskite absorber.<sup>55</sup>

Previous full molecular-dynamics simulation studies have extensively modeled the formation of vapor-deposited films depending on deposition rate, incidence angle, substrate temperature, and in particular the substrate type.<sup>52,54,56–61</sup> As depicted in Figure 4E,F, the



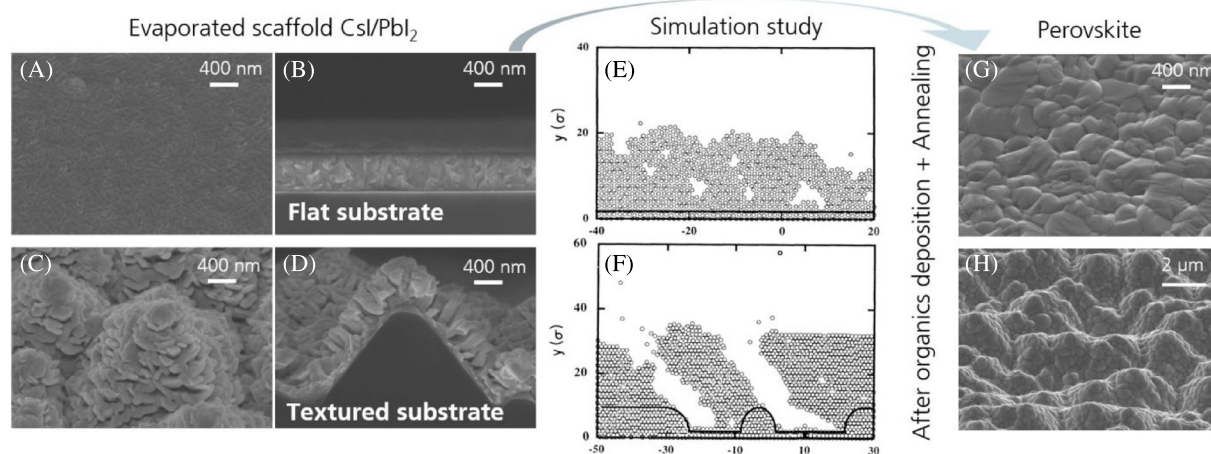


**FIGURE 4** Influence of the substrate roughness on the evaporated scaffold formation and the perovskite morphology. Scanning electron microscopy (SEM) images of the  $\text{PbI}_2/\text{CsI}$  scaffold (10% rate ratio) formed on top of (A, B) flat substrate and (C, D) textured substrate. (E, F) Full molecular-dynamics simulation study depicting vapor-deposited film formation depending on the substrate's surface roughness (reprint with permission from journal<sup>54</sup>). SEM top-view images of perovskite on top of G) flat substrate and H) textured substrate.

results of the numerical simulation study carried out by Paik and colleagues reproduce to a large extent our experimental observations.<sup>54</sup> When introducing a surface roughness, the vapor-deposited film is characterized by a columnar growth and the layer is more porous (Figure 4F). This observed porosity can be explained by the “shadowing” effect.<sup>52,54,56</sup> During the growth of obliquely deposited films, the highest features of the film (in our case the pyramid tips) will geometrically shadow other surfaces of the film from direct impingement by the incoming vapor flux.<sup>60</sup> The self-shadowing mechanism leads to voids within the film and, under conditions of collimated vapor flux, an elongated columnar structure. Furthermore, the shadowing effect means that the peaks receive a greater deposition flux than the valleys.<sup>56</sup> Thus, instead of the film growing at a uniform rate, the growth rate is faster at the pyramid tip than in the valleys.<sup>56</sup> This explains why the thickness of the evaporated scaffold (and subsequently the thickness of the perovskite) on the tip is always larger than the side.

Besides the shadowing effect, the increased surface area of textured silicon in comparison to planar silicon results in a thinner thickness of the evaporated film on the former. Here, the concept of a texture factor is used to describe this geometric difference. It is defined as the ratio between film thickness on a planar substrate to that on a textured substrate and has a value greater than 1.

Besides surface roughness, numerical simulation studies have shown that increasing the deposition angle, or reducing the substrate temperature, can also enhance the evaporated film's porosity (not tested in our experimental study).<sup>54,56–58,61</sup> These insights become important to take into consideration when, for example, thinking about designing large evaporation chambers to upscale the hybrid route for fully textured perovskite silicon tandem solar cells.

The top-view SEM images in Figure 4G,H show that upon the deposition of organics via spin-coating and annealing, the perovskite layer is uniform on the flat substrate and conformal on the textured substrate (no voids or bare silicon tips can be spotted). Moreover, the apparent grain size is on the order of 250–350 nm in both variations.

The discussed importance of scaffold porosity is evident when investigating the structural quality of the perovskite films. By depositing a similar solution in the second step on the two scaffolds and annealing, full conversion to the perovskite phase is observed on textured silicon, whereas an additional high  $\text{PbI}_2$  signal is detected on the flat substrate (Figure S4). This impurity originates from the non-optimal perovskite conversion (limited solution infiltration due to limited porosity of the 550 nm thick scaffold) as will be further discussed in Section 3.3.

Next to the morphological quality, the perovskite elemental distribution on a textured substrate should be well controlled to reduce non-radiative recombination losses at, for example, defect sites in the bulk or at the surface.<sup>62</sup> Moreover, while for solution-processed perovskite absorbers, the weighed-in precursor quantities are used to estimate the final perovskite film composition, such an approach is not applicable to the hybrid route. Using time-of-flight secondary ion mass spectrometry (ToF-SIMS) and X-ray photoelectron spectroscopy (XPS), we shed light on differences between perovskite absorbers synthesized on a textured vs a flat substrate.

X-ray photoelectron spectroscopy measurements conducted along the absorber's depth show a similar bulk composition for the perovskite films synthesized on textured and flat substrates (Figure S5). More precisely, the halide ratio is found to be  $\text{I}:\text{Br} \sim 78:22$  (Figure S5a) and the  $\text{Cs}:\text{Pb}$  ratio is nearly 15:85 (Figure S5b). From this, we estimate a perovskite bulk composition  $\text{FA}_{0.85}\text{Cs}_{0.15}\text{Pb}(\text{I}_{0.78}\text{Br}_{0.22})_3$  for the 1.66 eV absorbers.

Furthermore, while the performed XPS investigation was carried out on static samples, we noted that the compositional investigation of perovskite films on a textured substrate becomes more accurate by introducing an azimuthal substrate rotation ( $\sim 30$ – $60$  rpm) during the measurement. By carrying out ToF-SIMS measurements, Figure S6a shows no significant difference with the rotation variation on a flat substrate. In contrast, a shift in the detected signals can be noted by introducing rotation in the textured substrate (Figure S6b). This is due

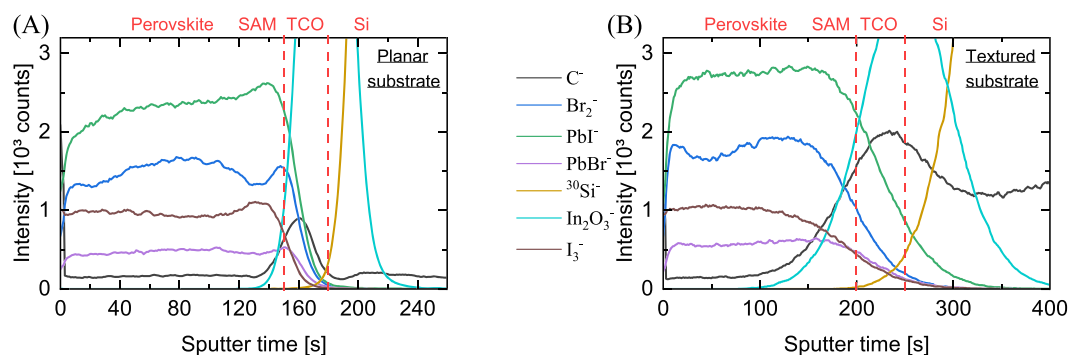


**FIGURE 5** Influence of the substrate roughness on the perovskite elemental composition. Elemental distribution of perovskite ions (among others) along the thickness on top of (A) a planar substrate and (B) a textured substrate, derived from ToF-SIMS measurements.  $I_3^-$  and  $Br_2^-$  were investigated instead of their monoatomic ions due to the high ion intensity of those species that lead to detector saturation.

to the lower influence of exponential tails caused by the shading of ion beams which allows resolving additional features in the depth, for example, gradients and presence of the SAM molecule (Figure 5).

Using the substrate rotation variation on both flat and textured silicon, a simultaneous increase in  $PbI^-$  and  $I_3^-$  signals can be observed at the interface between the perovskite absorber formed on a planar substrate and the underlying 2PACz layer (Figure 5A). Such a behavior is not observed on the textured substrate (Figure 5B). This indicates a clustering of unreacted  $PbI_2$  at the bottom interface, which is in accordance with the performed XRD structural analysis (Figure S4). Furthermore, we note a larger increment in the  $C^-$  signal in the textured substrate, which we ascribe to the higher 2PACz concentration used (7 mmol instead of 1.2 mmol) to ensure full 2PACz coverage on the textured substrate.

The morphological investigations with a link to former numerical simulation reports hence demonstrate the inherent porosity enhancement of evaporated  $CsI/PbI_2$  films on a rough substrate. Accurate compositional investigations (depth profiling using ToF-SIMS and XPS with substrate rotation) and structural investigations point out that the enhanced porosity is a required attribute for the growth of a homogeneous perovskite composition when employing the hybrid perovskite deposition route.

### 3.3 | Strategies for perovskite phase purity and photostability

Generally, perovskite absorbers processed with the hybrid evaporation/spin-coating method are prone to impurity accumulation/formation in case of imbalance between evaporated inorganic compounds and wet-chemically deposited compounds. One way to ensure the formation of a homogeneous absorber (without phase impurities) is to increase the evaporated scaffold porosity as discussed in the previous section. Besides this strategy, in this section we investigate three pathways, based on the  $A^+$  site cation engineering scheme, to improve the perovskite conversion and ensure a good photostability of the absorber.

X-ray diffraction measurements of perovskite films synthesized with different  $CsI:PbI_2$  evaporation rate ratios are depicted in Figure 6A. Besides the perovskite cubic phase, the reference absorber ( $CsI:PbI_2 = 10\%$ ) exhibits a high  $PbI_2$  signal shown by the characteristic peaks at  $12.7^\circ$ ,  $38.7^\circ$ , and  $52.4^\circ$  (corresponding to the (001), (003), and (004) lattice planes).<sup>63,64</sup> Looking at the film morphology, the cross-sectional SEM image (Figure 6F) indicates that the  $PbI_2$  is localized at the interface with the charge transport layer (2PACz). A similar observation can be noted in the reference perovskite film on a textured substrate (red arrows in Figure S7b, and grey-colored X-ray diffractogram in Figure S7c). This is critical on the solar cell level as the Insulating nature of  $PbI_2$  will impede charge extraction/transfer, as will be demonstrated later in this section. In addition, the incomplete reaction (presence of remnant  $PbI_2$ ) entails a reduced perovskite thickness, and hence a lower photon absorption.

With the hypothesis of a high  $A^+$  site cation deficiency at the bottom part of the reference perovskite absorber, we increase the  $CsI:PbI_2$  evaporation rate ratio from 10% to 12%, then 15%. With that, the  $Cs:Pb$  atomic ratio in the scaffold increases gradually from an average of 15 atm% to 18 atm% to 22 atm%, respectively, as derived from X-ray photoelectron spectroscopy measurements (Figure S8). As a result, X-ray diffractograms show a steady decrease in the  $PbI_2$  signal (Figure 6A). Certainly, a higher  $Cs^+$  content in the evaporated scaffold will lead to further intercalation of cations in the perovskite structure and enhance the conversion rate. To confirm that this effect is solely stemming from  $Cs^+$  incorporation, we carry out a similar experiment but with a variation in  $CsBr:PbI_2$  evaporation rate ratio. Similar observations can be noted as displayed in Figure S3a (green-, purple-, and yellow-colored X-ray diffractograms). Nevertheless, while the perovskite conversion is enhanced, continuous steady-state photoluminescence (PL) measurements reveal that a high incorporation of cesium compromises the photostability (Figure 6E). This can be seen with the higher deviation rate of the PL peak position and height over the course of the 300 s laser illumination period. In contrast, the reference perovskite with low  $Cs^+$  ( $CsI:PbI_2 = 10\%$ ) shows a relatively stable PL signal over the same duration. The adverse impact of high cesium incorporation has been previously pointed out in a number of

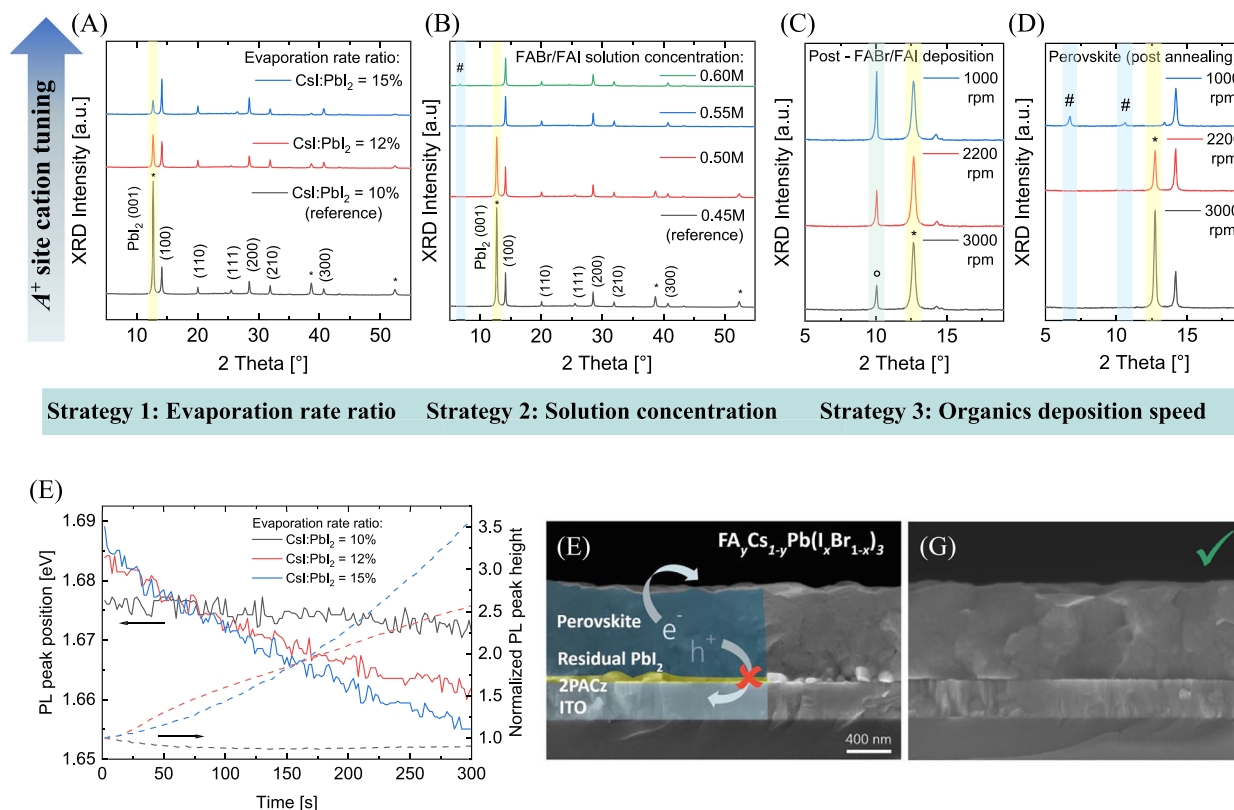


**FIGURE 6** Strategies to achieve a high perovskite phase purity and mitigate phase impurities. X-ray diffraction (XRD) measurements of perovskite absorbers with variation in (A) the CsI:PbI<sub>2</sub> evaporation rate ratio (strategy 1), (B) the organohalide solution concentration (strategy 2), and (C,D) the organohalide deposition speed (strategy 3). In (C) the XRD measurements are taken directly after organics deposition (i.e., before the annealing treatment). The #, °, and \* signals designate extra organic, intermediate phase, and PbI<sub>2</sub> phases, respectively. The thickness of the scaffold was set to 300 nm. (E) Evolution of the photoluminescence (PL) peak position and normalized height as a function of the CsI:PbI<sub>2</sub> evaporation rate ratio under 1-sun equivalent laser intensity. Cross-section scanning electron microscopy (SEM) images of perovskite films (F) with and (G) without remnant PbI<sub>2</sub> at the interface.

studies where the perovskite was processed via the standard 1-step wet-chemical technique.<sup>65–68</sup> With the hybrid route, we confirm a similar behavior.

To avoid compromising photostability, we pursue full perovskite conversion by increasing the amount of the other cation in the system (formamidinium). This can be achieved by either increasing the organohalide solution concentration or lowering the spin-coating speed. In principle, with the former strategy, a higher solution concentration enables the infiltration of a larger amount of FA<sup>+</sup> molecules for a similar retained solution volume by the scaffold. Figure 6B shows that by increasing the solution concentration in 0.05 M steps, the PbI<sub>2</sub> signal is systematically reduced and the optimal structural composition is achieved with 0.55 M. The perovskite layer morphology is more homogeneous, and no remnant PbI<sub>2</sub> is visible at the interface with the underlying charge transport layer (Figure 6G). Beyond full conversion, one can note that further increasing the solution concentration can result in the formation of excess organic phases, most probably on top of the perovskite surface (XRD peak at  $2\theta = 6.74^\circ$  and  $10.62^\circ$ ). This is detrimental as additional organic phases are hygroscopic and accelerate the reaction with humidity, which can lead to perovskite degradation.

Increasing the amount of infiltrated FA<sup>+</sup> molecules can alternatively be done by reducing the spin-coating speed. By investigating the structural composition of the films directly after FABr/FAI solution deposition (i.e., before the annealing step), Figure 6C shows that reducing the spin-coating speed from 3,000 rpm to 1,000 rpm increases the intensity of the intermediate phase (peak at  $2\theta = 10.1^\circ$ ).<sup>69,70</sup> Consequently, the residual PbI<sub>2</sub> density in the final perovskite film is gradually decreased (Figure 6D).

Looking one step ahead, due to the common approach of solution infiltration within a porous evaporated template, we expect that the derived learnings, in particular the deposition speed strategy (for ensuring full perovskite conversion) to be transferrable to, for example, slot-die coating, spray-coating, inkjet-printing and other scalable wet-chemical coating techniques for deposition on large areas. Finally, we note that while the three discussed strategies to ensure full perovskite conversion were demonstrated on flat substrates, we observe a similar behavior on textured silicon as can be seen in Figure S7c (impact of organohalide solution concentration) and in Figure 7B (impact of solution deposition speed).

To investigate the impact of remnant precursors on device performance, perovskite single-junction solar cells on flat substrates are



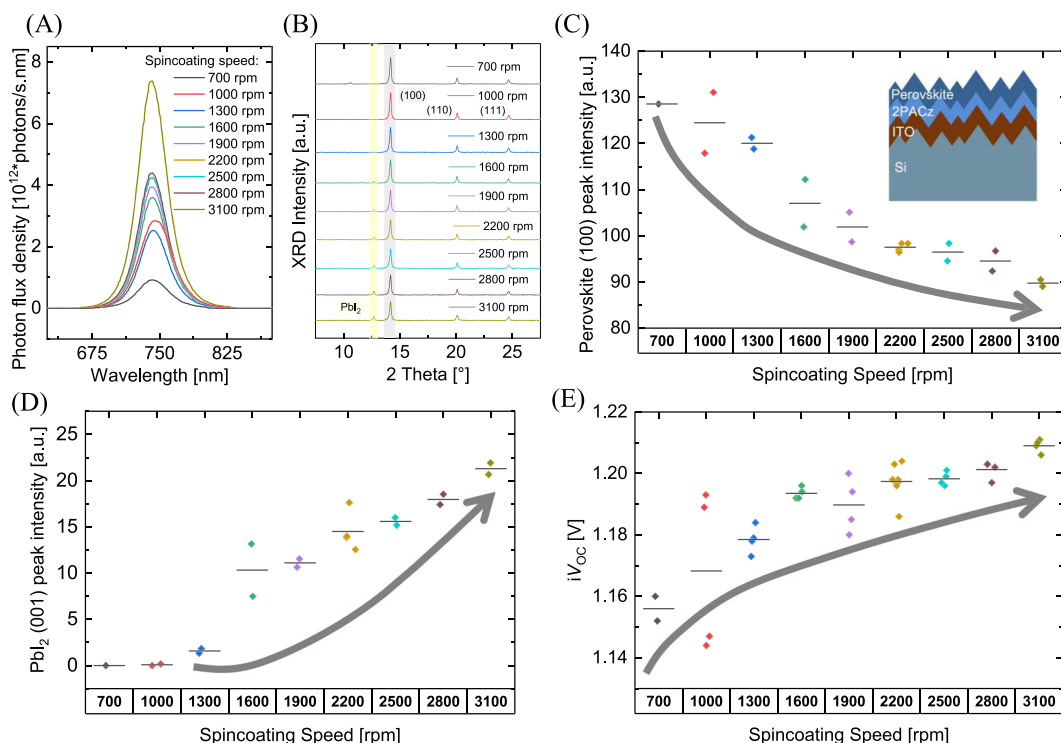


**FIGURE 7** Influence of remnant  $\text{PbI}_2$  on perovskite photoluminescence and implied open-circuit voltage ( $iV_{\text{OC}}$ ). (A) Absolute photoluminescence (PL) response and (B) X-ray diffraction (XRD) measurements of perovskite absorbers on textured silicon with a variation in spin-coating speed of the deposited organohalides to intentionally control the density of remnant  $\text{PbI}_2$ . Evolution of (C) the main perovskite diffraction peak (100) intensity, (D) the main  $\text{PbI}_2$  diffraction peak (001) intensity, and (E) the extracted  $iV_{\text{OC}}$  (from PL) of the perovskite stack as a function of the organohalide deposition speed.

fabricated with a variation in organohalide solution deposition speed. Accordingly, films with the two extremes are intentionally formed: large density of remnant  $\text{PbI}_2$  at the bottom interface (4,000 rpm) and excess organic phases at the top interface (1,000 rpm). The current-density voltage ( $jV$ ) curve photovoltaic metrics are displayed in Figure S9. Most notably, the power conversion efficiency of the devices with the lowest (1,000 rpm) and highest (4,000 rpm) solution deposition speed is below 4%. Looking more in detail at a typical  $jV$  curve from the two variations, on the one hand, a low shunt resistance is observed to limit the device performance in the case of low spin-coating speed. This indicates that excess organic phases on top of the perovskite surface (as revealed by XRD, Figure 6D) could indeed lead to the absorber's degradation and thereby increase the detrimental shunt paths. On the other hand, a severe S-shape and hysteresis can be noted in the  $jV$  curves from the samples fabricated with a high spin-coating speed. We ascribe this observation to a high density of unconverted  $\text{PbI}_2$  at the bottom interface (as revealed by XRD, Figure 6D) which impedes charge extraction at the perovskite/2PACz junction. The optimum performance in this batch was obtained with 2,200 rpm due to the elimination of excess organic phases. However, it is important to still highlight the hysteresis in the  $jV$  curves as well as the limited performance, which we ascribe mainly, but among other factors, to the residual  $\text{PbI}_2$  (XRD in Figure 6D). By further tuning the perovskite conversion (optimum of previously discussed process parameters), Figure S10a shows that

the PCE for these single-junction solar cells can be enhanced from 12.7% to 14.3% (reverse scan). Moreover, the device shows a good operational stability over 100 hours under 1-sun illumination in air (Figure S10b).

### 3.4 | Interplay between remnant $\text{PbI}_2$ and photoluminescence response: a misleading route

To date, most reports on perovskite solar cells with high  $V_{\text{OC}}$  and high PCE introduce excess  $\text{PbI}_2$  into the perovskite precursor solution.<sup>71-73</sup> To understand the impact of this strategy, extensive studies from the community have led to the following common consensus: excess  $\text{PbI}_2$  sits at the perovskite grain boundaries and interfaces ensuring an efficient passivation of the defects.<sup>74-83</sup> As a result, an enhancement in the  $jV$  metrics and particularly the  $V_{\text{OC}}$  of the solar cell is achieved. On the perovskite absorber level, the  $\text{PbI}_2$  excess-based enhancement is usually reflected by an increase in the absolute photoluminescence (PL) intensity in comparison to the perovskite without excess  $\text{PbI}_2$ . With the hybrid route however, as presented in Section 2.3, excess  $\text{PbI}_2$  rather remains unreacted under the perovskite film due to the nature of the two-step heterogeneous (solid-liquid) perovskite formation process. Consequently, from an optimization point of view, only analyzing the photoluminescence response as a metric to qualify the perovskite optoelectronic quality is insufficient.

Figure 7A,B shows the absolute photoluminescence (PL) response and X-ray diffractogram of perovskite absorbers deposited on textured silicon with a variation in organohalide solution deposition speed to intentionally control the density of residual  $\text{PbI}_2$ . By increasing the deposition speed, the perovskite main peak intensity (100) decreases gradually. Simultaneously, the  $\text{PbI}_2$  main peak intensity (001) shows a consistent increase. In parallel to the structural changes, optoelectronic investigation using absolute photoluminescence spectroscopy reveals an increase in the PL intensity (Figure 7A) as well as the extracted implied open-circuit voltage ( $iV_{\text{OC}}$ ) of the perovskite/2PACz/ITO/textured Si stack (Figure 7E). Figure S11 shows that all perovskite variations display a similar PL peak position as well as a comparable full-width-half-maximum (FWHM) and peak position of the (100) perovskite peak in XRD, thereby ruling out, for example, bandgap enlargement or an improvement in perovskite structural quality as potential reasons behind the enhanced  $iV_{\text{OC}}$ . We therefore conclude that increasing the density of  $\text{PbI}_2$  in the final perovskite film for the hybrid route is the main reason behind the enhanced  $V_{\text{OC}}$  potential. Our observations align with the existing literature on solution-processed perovskite absorbers with excess  $\text{PbI}_2$ .

Nevertheless, we reveal that only relying on absolute PL as a characterization tool can give a misleading optimization route. From

this perspective and looking at the commercialization prospects of fully textured tandems, standard  $iV_{\text{OC}}$  imaging methods which are used as a quick metric to assess the absorber's quality should be complemented by structural investigations (e.g., XRD) to probe the density of remnant  $\text{PbI}_2$  as well as electric methods (e.g.,  $jV$  characterization) to investigate charge extraction.

### 3.5 | Implementation in a Monolithic Fully Textured Perovskite Silicon Tandem Solar Cell Architecture

The optimized top cell absorber  $\text{FA}_{0.15}\text{Cs}_{0.85}\text{Pb}(\text{I}_{0.78}\text{Br}_{0.22})_3$  with a  $\sim 630$  nm thickness and  $\sim 1.66$  eV bandgap was implemented in a monolithic fully textured perovskite silicon tandem solar cell architecture. For the perovskite sub-cell, a  $p$ - $i$ - $n$  configuration was adopted, with the self-assembling-molecule 2PACz as a hole transport layer and the standard  $\text{C}_{60}/\text{SnO}_x/\text{ITO}$  top contact (Figure 8A). The bottom sub-cell consisted of a silicon heterojunction with a textured front and textured back surface. Figure S12 displays the distribution of pyramid sizes on the front side. An average size of  $1.5 \mu\text{m}$  was derived via LEXT optical microscope measurements. Furthermore, a

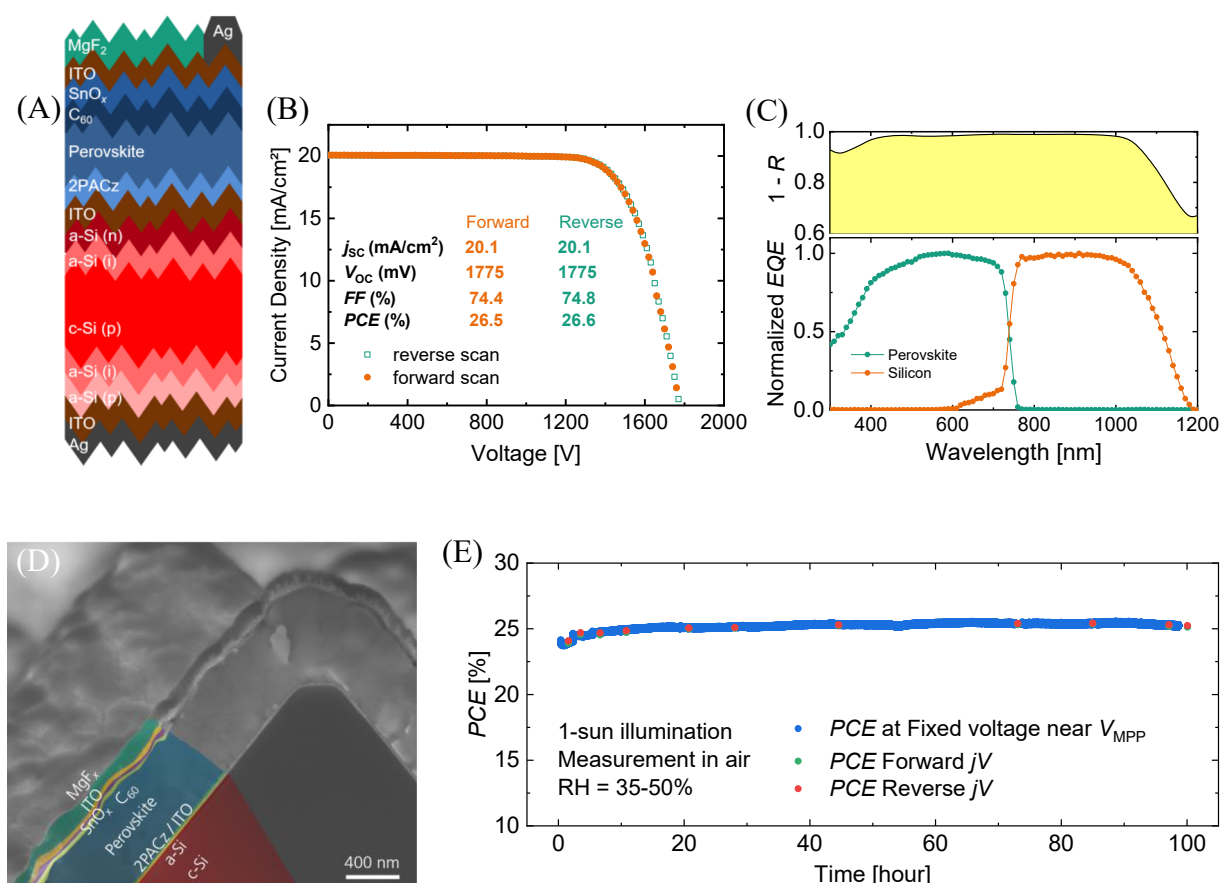


**FIGURE 8** Implementation of a monolithic fully textured perovskite silicon tandem solar cell. (A) Schematic of the monolithic tandem solar cell architecture with an active area of  $1 \text{ cm}^2$ . (B) Current density-voltage ( $jV$ ), (C) external quantum efficiency (EQE) and reflectance, (D) cross-section scanning electron microscopy (SEM) image, and (E) operational stability test of a fully textured perovskite silicon tandem solar cell (stability test: different sample with same architecture). [Correction added on 26 January 2024, after first online publication: Figure 8 has been corrected in this version.]

high conformality of the integrated perovskite absorber as well as the adjacent layers can be noted from the cross-sectional SEM image of the tandem device (Figure 8D).

With a meticulous control of the hybrid route's intrinsic deposition parameters, and without employing additional crystallization/bulk defect passivation agents or surface passivation layers, a stabilized power conversion efficiency of 26.5% (1 cm<sup>2</sup> active area) was achieved (Figure S13). The statistics on the device performance can be seen in Figure S14. Notably, a high short-circuit current density of 20.1 mA cm<sup>-2</sup> is obtained, which mainly stems from the reduced reflection along the spectrum using the textured substrate as can be seen in Figure 8C. This is also reflected in the external quantum efficiency (EQE) measurements, which show no particular dips in both the perovskite and silicon wavelength regions. In addition to the good performance, the optimized absorber enabled a good operational stability by conserving 100% of the initial power output of the tandem cell when stressed in air under 1-sun illumination intensity, with a relative humidity RH = 35–50% and a stage temperature of 25°C (Figure 8E). The test was stopped after 100 hours to avoid overheating of the lamps of the sun simulator setup; future studies with dedicated setups need to be carried out to fully assess the stability following ISOS procedures.<sup>84</sup> Still overall, the fully textured perovskite silicon tandem solar cell showcases a comparable stability to the single-junction perovskite solar cell (see Section 2.3), which demonstrates the transferability of optimized process parameters from flat to textured substrates.

## 4 | CONCLUSION

In this study, we analyze the influence of the hybrid route process parameters on the formation of methylammonium-free wide-bandgap perovskite absorbers on industrial textured silicon versus flat substrates. Using various characterization tools, we identify sources of optoelectronic, structural, morphological, and electrical deficiency and offer ideas to tackle them. Besides the previously reported use of organohalide solution mixing to tune the optical bandgap, we reveal a critical solution mixture regime where dendritic perovskite formation occurs, which can lead to detrimental shunting paths. In addition, we find that shunt paths are likely to be exacerbated if excess organic phases are present on top of the perovskite surface due to non-optimal balance between evaporated inorganic compounds and wet-chemically deposited organic compounds. In case of a deficit of the organic molecules, PbI<sub>2</sub> tends to accumulate at the perovskite bottom side. While this results in a severe limitation in the charge extraction capability at the adjacent interface, we notice an enhanced photoluminescence response with higher remnant PbI<sub>2</sub> density. We therefore shed light on the importance of careful analysis of PL data as well as the need to complement optoelectronic investigations with supplemental structural (XRD) and electrical characterization (jV) for hybrid route processed perovskite absorbers to avoid a misleading optimization direction. To enable full perovskite conversion, strategies based on the A<sup>+</sup> cation engineering scheme, targeting an increase of the

concentration of FA<sup>+</sup> in the solution step or Cs<sup>+</sup> in the evaporation step, especially at the bottom part of the evaporated scaffold, are studied. While both strategies efficiently reduce the density of impurities, we find that a high amount of cesium in the perovskite composition compromises its photostability. By tuning the intrinsic hybrid route deposition parameters, the integration of the optimized perovskite absorber in a tandem solar cell architecture using an industrial texturing process successfully yields a stabilized power conversion efficiency of 26.5% and a good operational stability. In conclusion, this work strengthens the understanding of perovskite film formation for fully textured perovskite silicon tandem solar cells and provides comprehensive guidelines for future work on upscaling perovskite top cell fabrication to meet industry needs.

## ACKNOWLEDGEMENTS

This work was funded by the Fraunhofer Lighthouse Project MaNiTU as well as the German Federal Ministry for Economic Affairs and Climate Action under contract no. 03EE1086A (PrEstO). The authors thank K. Fischer and J. Myers for technical support, J. Zielonka for her support with SEM measurements, K. Abrorov and A. Gonzalez Abad for their support with EQE measurements, A. Reinholdt and A. Schmitt for XPS measurements, and F. Martin and M. Mahmoud for their support with reflection and UV-vis measurements. Open Access funding enabled and organized by Projekt DEAL.

## DATA AVAILABILITY STATEMENT

The data that support the findings of this study are available from the corresponding author upon reasonable request.

## ORCID

Oussama Er-raji  <https://orcid.org/0000-0003-2128-9467>

Alexander J. Bett  <https://orcid.org/0000-0003-0312-6701>

Stefan W. Glunz  <https://orcid.org/0000-0002-9877-2097>

## REFERENCES

1. NREL. *Best Research-Cell Efficiency Chart*.
2. Liu J, de Bastiani M, Aydin E, et al. Efficient and stable perovskite-silicon tandem solar cells through contact displacement by MgFx. *Science* (New York, NY). 2022;377(6603):302–306. doi:10.1126/science.abn8910
3. Hou Y, Aydin E, de Bastiani M, et al. Efficient tandem solar cells with solution-processed perovskite on textured crystalline silicon. *Science*. 2020;367(6482):1135–1140. doi:10.1126/science.aaz3691
4. Isikgor FH, Furlan F, Liu J, et al. Concurrent cationic and anionic perovskite defect passivation enables 27.4% perovskite/silicon tandems with suppression of halide segregation. *Joule*. 2021;5(6):1566–1586. doi:10.1016/j.joule.2021.05.013
5. Tockhorn P, Sutter J, Cruz A, et al. Nano-optical designs for high-efficiency monolithic perovskite-silicon tandem solar cells. *Nat Nanotechnol*. 2022;17(11):1214–1221. doi:10.1038/s41565-022-01228-8
6. Harter A, Mariotti S, Korte L, Schlattmann R, Albrecht S, Stannowski B. Double-sided nano-textured surfaces for industry compatible high-performance silicon heterojunction and perovskite/silicon tandem solar cells. *Prog Photovoltaics*. 2023;31(8):813–823. doi:10.1002/ppv.3685
7. Zheng J, Wei H, Ying Z, et al. Balancing charge-carrier transport and recombination for perovskite/TOPCon tandem solar cells with

- double-textured structures. *Adv Energy Mater.* 2023;13(5):2203006. doi:[10.1002/aenm.202203006](https://doi.org/10.1002/aenm.202203006)
8. Jäger K, Sutter J, Hammerschmidt M, Schneider P-I, Becker C. Prospects of light management in perovskite/silicon tandem solar cells. *Nanophotonics*. 2021;0(8):1991-2000. doi:[10.1515/nanoph-2020-0674](https://doi.org/10.1515/nanoph-2020-0674)
  9. Xu Q, Zhao Y, Zhang X. Light management in monolithic perovskite/silicon tandem solar cells. *Sol RRL*. 2019;173(2):1900206. doi:[10.1002/solr.201900206](https://doi.org/10.1002/solr.201900206)
  10. Hossain MI, Qarony W, Ma S, Zeng L, Knipp D, Tsang YH. Perovskite/silicon tandem solar cells: from detailed balance limit calculations to photon management. *Nano-Micro Lett.* 2019;11(1):58. doi:[10.1007/s40820-019-0287-8](https://doi.org/10.1007/s40820-019-0287-8)
  11. Callies A, Hanser M, Goldschmidt JC, Bläsi B, Höhn O. Structuring of perovskite-silicon tandem solar cells for reduced reflectance and thermalization losses. *Opt Express*. 2023;31(12):19428-19442. doi:[10.1364/OE.491371](https://doi.org/10.1364/OE.491371)
  12. Gota F, Schmager R, Farag A, Paetzold UW. Energy yield modelling of textured perovskite/silicon tandem photovoltaics with thick perovskite top cells. *Opt Express*. 2022;30(9):14172-14188. doi:[10.1364/OE.447069](https://doi.org/10.1364/OE.447069)
  13. Tucher N, Höhn O, Murthy JN, et al. Energy yield analysis of textured perovskite silicon tandem solar cells and modules. *Opt Express*. 2019;27(20):A1419-A1430. doi:[10.1364/OE.27.0A1419](https://doi.org/10.1364/OE.27.0A1419)
  14. Lehr J, Langenhorst M, Schmager R, Kirner S, Lemmer U, Richards BS, Case C, Paetzold UW. *Energy Yield Modelling of Perovskite/Silicon Two-Terminal Tandem PV Modules with Flat and Textured Interfaces*. under review.
  15. Roß M, Severin S, Stutz MB, et al. Co-evaporated formamidinium lead iodide based perovskites with 1000 h constant stability for fully-textured monolithic perovskite/silicon tandem solar cells. *Adv Energy Mater.* 2021;11(35):2101460. doi:[10.1002/aenm.202101460](https://doi.org/10.1002/aenm.202101460)
  16. Schulze PSC, Wienands K, Bett AJ, et al. Perovskite hybrid evaporation/spin coating method: from band gap tuning to thin film deposition on textures. *Thin Solid Films*. 2020;704:137970. doi:[10.1016/j.tsf.2020.137970](https://doi.org/10.1016/j.tsf.2020.137970)
  17. Sahli F, Werner J, Kamino BA, et al. Fully-textured monolithic perovskite/silicon tandem solar cells with 25.2% power conversion efficiency. *Nat Mater*. 2018;17(9):820-826. doi:[10.1038/s41563-018-0115-4](https://doi.org/10.1038/s41563-018-0115-4)
  18. Er-raji O, Rustam L, Kore BP, Glunz SW, Schulze PSC. Insights into perovskite film formation using the hybrid evaporation/spin-coating route: an in situ XRD study. *ACS Appl Energy Mater.* 2023;6(11):6183-6193. doi:[10.1021/acsaem.3c00698](https://doi.org/10.1021/acsaem.3c00698)
  19. Nogay G, Sahli F, Werner J, et al. 25.1%-Efficient monolithic perovskite/silicon tandem solar cell based on a p-type monocrystalline textured silicon wafer and high-temperature passivating contacts. *ACS Energy Lett.* 2019;4(4):844-845. doi:[10.1021/acsenerylett.9b00377](https://doi.org/10.1021/acsenerylett.9b00377)
  20. Luo X, Luo H, Li H, et al. Efficient perovskite/silicon tandem solar cells on industrially compatible textured silicon. *Adv Mater (Deerfield Beach, Fla)*. 2023;35(9):e2207883. doi:[10.1002/adma.202207883](https://doi.org/10.1002/adma.202207883)
  21. Li Y, Shi B, Xu Q, et al. Wide bandgap interface layer induced stabilized perovskite/silicon tandem solar cells with stability over ten thousand hours. *Adv Energy Mater.* 2021;11(48):2102046. doi:[10.1002/aenm.202102046](https://doi.org/10.1002/aenm.202102046)
  22. Xu Q, Shi B, Li Y, et al. Conductive passivator for efficient monolithic perovskite/silicon tandem solar cell on commercially textured silicon. *Adv Energy Mater.* 2022;12(46):2202404. doi:[10.1002/aenm.202202404](https://doi.org/10.1002/aenm.202202404)
  23. Yan L, Li Y, Shi B, et al. Reducing electrical losses of textured monolithic perovskite/silicon tandem solar cells by tailoring nanocrystalline silicon tunneling recombination junction. *EuroSun2004*. 2022;245:111868. doi:[10.1016/j.solmat.2022.111868](https://doi.org/10.1016/j.solmat.2022.111868)
  24. He Y, Tang Z, He B, et al. Composition engineering of perovskite absorber assisted efficient textured monolithic perovskite/silicon heterojunction tandem solar cells. *RSC Adv*. 2023;13(12):7886-7896. doi:[10.1039/d2ra05481g](https://doi.org/10.1039/d2ra05481g)
  25. Mao L, Yang T, Zhang H, et al. Fully-textured, production-line compatible monolithic perovskite/silicon tandem solar cells approaching 29% efficiency. *Adv Mater (Deerfield Beach, Fla)*. 2022;34(40):e2206193. doi:[10.1002/adma.202206193](https://doi.org/10.1002/adma.202206193)
  26. Schultz-Wittmann O., Schulze P.S.C., Er-Raji O., Efinger R., Kabakl S., Heydarian M., McMullin K.A., Fischer O., Bett A.J., Erath D., Pingel S., Heitmann U., Kiaee Z., Kohlstdt M., Kore B.P., Nagel H., Schubert M.C., Bivour M., Goldschmidt J.C., Borchert J., Hermle M., Glunz S.W.. *Upscaling of Perovskite-Silicon Tandem Solar Cells*. In:
  27. Grohe A, Nekarda J-F, Schultz O. *Verfahren zur Metallisierung von Solarzellen und dessen Verwendung*
  28. Er-raji O, Messmer C, Bett AJ, et al. Loss analysis of fully-textured perovskite silicon tandem solar cells: characterization methods and simulation towards the practical efficiency potential. *Sol RRL*. 2023. doi:[10.1002/solr.202300659](https://doi.org/10.1002/solr.202300659)
  29. Tauc J, Grigorovici R, Vancu A. Optical properties and electronic structure of amorphous germanium. *Phys Status Solidi B*. 1966;15(2):627-637. doi:[10.1002/pssb.19660150224](https://doi.org/10.1002/pssb.19660150224)
  30. Meusel M, Adelhelm R, Dimroth F, Bett AW, Warta W. Spectral mismatch correction and spectrometric characterization of monolithic III-V multi-junction solar cells. *Progr Photovoltaics: Res Applic*. 2002;10(4):243-255. doi:[10.1002/pip.407](https://doi.org/10.1002/pip.407)
  31. Heydarian M, Messmer C, Bett AJ, et al. Maximizing current density in monolithic perovskite silicon tandem solar cells. *Solar RRL*. 2023;7(7):2200930. doi:[10.1002/solr.202200930](https://doi.org/10.1002/solr.202200930)
  32. Saliba M, Matsui T, Seo J-Y, et al. Cesium-containing triple cation perovskite solar cells: improved stability, reproducibility and high efficiency. *Energ Environ Sci*. 2016;9(6):1989-1997. doi:[10.1039/C5EE03874J](https://doi.org/10.1039/C5EE03874J)
  33. Tan W, Bowring AR, Meng AC, McGehee MD, McIntyre PC. Thermal stability of mixed cation metal halide perovskites in air. *ACS Appl Mater Interfaces*. 2018;10(6):5485-5491. doi:[10.1021/acsami.7b15263](https://doi.org/10.1021/acsami.7b15263)
  34. Mahboubi Soufiani A, Yang Z, Young T, et al. Impact of microstructure on the electron-hole interaction in lead halide perovskites. *Energ Environ Sci*. 2017;10(6):1358-1366. doi:[10.1039/C7EE00685C](https://doi.org/10.1039/C7EE00685C)
  35. Schwenzer JA, Hellmann T, Nejand BA, et al. Thermal stability and cation composition of hybrid organic-inorganic perovskites. *ACS Appl Mater Interfaces*. 2021;13(13):15292-15304. doi:[10.1021/acsami.1c01547](https://doi.org/10.1021/acsami.1c01547)
  36. Brunetti B, Cavallo C, Ciccioli A, Gigli G, Latini A. On the thermal and thermodynamic (in)stability of methylammonium lead halide perovskites. *Sci Rep*. 2016;6(1):31896. doi:[10.1038/srep31896](https://doi.org/10.1038/srep31896)
  37. Conings B, Drijkoningen J, Gauquelin N, et al. Intrinsic thermal instability of methylammonium lead trihalide perovskite. *Adv Energy Mater.* 2015;5(15):1500477. doi:[10.1002/aenm.201500477](https://doi.org/10.1002/aenm.201500477)
  38. Philippe B, Park B-W, Lindblad R, et al. Chemical and electronic structure characterization of lead halide perovskites and stability behavior under different exposures—a photoelectron spectroscopy investigation. *Chem Mater*. 2015;5(5):1720-1731. doi:[10.1021/acs.chemmater.5b00348](https://doi.org/10.1021/acs.chemmater.5b00348)
  39. Schulze PSC, Bett AJ, Bivour M, et al. 25.1% High-efficient monolithic perovskite silicon tandem solar cell with a high band gap perovskite absorber. *Sol RRL*. 2020;4(7):2000152. doi:[10.1002/solr.202000152](https://doi.org/10.1002/solr.202000152)
  40. Lin Y-H, Sakai N, Da P, et al. A piperidinium salt stabilizes efficient metal-halide perovskite solar cells. *Science*. 2020;369(6499):96-102. doi:[10.1126/science.aba1628](https://doi.org/10.1126/science.aba1628)
  41. Akhil S, Akash S, Pasha A, et al. Review on perovskite silicon tandem solar cells: status and prospects 2T, 3T and 4T for real world conditions. *Mater Des*. 2021;211:110138. doi:[10.1016/j.matdes.2021.110138](https://doi.org/10.1016/j.matdes.2021.110138)
  42. Fu F, Li J, Yang TC-J, et al. Monolithic perovskite-silicon tandem solar cells: from the lab to fab? *Adv Mater (Deerfield Beach, Fla)*. 2022;34(24):e2106540. doi:[10.1002/adma.202106540](https://doi.org/10.1002/adma.202106540)



43. Cheng Y, Ding L. Perovskite/Si tandem solar cells: Fundamentals, advances, challenges, and novel applications. *Sus Mat*. 2021;1(3):324-344. doi:[10.1002/sus2.25](https://doi.org/10.1002/sus2.25)
44. Liu N, Wang L, Xu F, Wu J, Song T, Chen Q. Recent progress in developing monolithic perovskite/Si tandem solar cells. *Front Chem*. 2020;8:603375. doi:[10.3389/fchem.2020.603375](https://doi.org/10.3389/fchem.2020.603375)
45. Chen B, Ren N, Li Y, et al. Insights into the development of monolithic perovskite/silicon tandem solar cells. *Adv Energy Mater*. 2021;12(4):2003628. doi:[10.1002/aenm.202003628](https://doi.org/10.1002/aenm.202003628)
46. Eperon GE, Stranks SD, Menelaou C, Johnston MB, Herz LM, Snaith HJ. Formamidinium lead trihalide: a broadly tunable perovskite for efficient planar heterojunction solar cells. *Energ Environ Sci*. 2014;7(3):982-988. doi:[10.1039/c3ee43822h](https://doi.org/10.1039/c3ee43822h)
47. Noh JH, Im SH, Heo JH, Mandal TN, Seok SI. Chemical management for colorful, efficient, and stable inorganic-organic hybrid nanostructured solar cells. *Nano Lett*. 2013;13(4):1764-1769. doi:[10.1021/nl400349b](https://doi.org/10.1021/nl400349b)
48. Prasanna R, Gold-Parker A, Leijtens T, et al. Band gap tuning via lattice contraction and octahedral tilting in perovskite materials for photovoltaics. *J Am Chem Soc*. 2017;139(32):11117-11124. doi:[10.1021/jacs.7b04981](https://doi.org/10.1021/jacs.7b04981)
49. Bush KA, Frohna K, Prasanna R, et al. Compositional engineering for efficient wide band gap perovskites with improved stability to photo-induced phase segregation. *ACS Energy Lett*. 2018;3(2):428-435. doi:[10.1021/acsenenergylett.7b01255](https://doi.org/10.1021/acsenenergylett.7b01255)
50. Premkumar S, Kundu K, Umapathy S. Impact of cesium in methylammonium lead bromide perovskites: insights into the microstructures, stability and photophysical properties. *Nanoscale*. 2019;11(21):10292-10305. doi:[10.1039/c9nr02733e](https://doi.org/10.1039/c9nr02733e)
51. Sánchez S, Pfeifer L, Vlachopoulos N, Hagfeldt A. Rapid hybrid perovskite film crystallization from solution. *Chem Soc Rev*. 2021;50(12):7108-7131. doi:[10.1039/d0cs01272f](https://doi.org/10.1039/d0cs01272f)
52. Karabacak T. Thin-film growth dynamics with shadowing and re-emission effects. *J Nanophoton*. 2011;5(1):52501. doi:[10.1117/1.3543822](https://doi.org/10.1117/1.3543822)
53. Steinbach I. Effect of interface anisotropy on spacing selection in constrained dendrite growth. *Acta Mater*. 2008;56(18):4965-4971. doi:[10.1016/j.actamat.2008.06.009](https://doi.org/10.1016/j.actamat.2008.06.009)
54. Paik Sun M., Kim Sihong, Schuller Ivan K., and Ramirez R.. *Surface Kinetics and Roughness on Microstructure Formation in Thin Films*.
55. Duan X, Li X, Tan L, et al. Controlling crystal growth via an autonomously longitudinal scaffold for planar perovskite solar cells. *Adv Mater (Deerfield Beach, Fla)*. 2020;32(26):e2000617. doi:[10.1002/adma.202000617](https://doi.org/10.1002/adma.202000617)
56. Gholipour Shahraki M, Savaloni H. Thin-film-growth characteristics by computer simulation: nanostructural changes as a function of deposition conditions. *Phys Stat Sol (B)*. 2007;244(9):3115-3136. doi:[10.1002/pssb.200642198](https://doi.org/10.1002/pssb.200642198)
57. Dong L, Smith RW, Srolovitz DJ. A two-dimensional molecular dynamics simulation of thin film growth by oblique deposition. *J Appl Phys*. 1996;80(10):5682-5690. doi:[10.1063/1.363621](https://doi.org/10.1063/1.363621)
58. Smith Richard W. and Srolovitz David J.. *Void Formation During Film Growth: A Molecular Dynamics Simulation Study*.
59. Whitacre JF, Rek ZU, Bilello JC, Yalisove SM. Surface roughness and in-plane texturing in sputtered thin films. *J Appl Phys*. 1998;84(3):1346-1353. doi:[10.1063/1.368204](https://doi.org/10.1063/1.368204)
60. Vicka D, Friedricha LJ, Dewa SK, et al. Self-shadowing and surface diffusion effects in obliquely deposited thin films. *Thin Solid Films*. 1999;339(1-2):88-94. doi:[10.1016/S0040-6090\(98\)01154-7](https://doi.org/10.1016/S0040-6090(98)01154-7)
61. Müller K-H. Dependence of thin-film microstructure on deposition rate by means of a computer simulation. *J Appl Phys*. 1985;58(7):2573-2576. doi:[10.1063/1.335885](https://doi.org/10.1063/1.335885)
62. Macpherson S, Doherty TAS, Winchester AJ, et al. Local nanoscale phase impurities are degradation sites in halide perovskites. *Nature*. 2022;607(7918):294-300. doi:[10.1038/s41586-022-04872-1](https://doi.org/10.1038/s41586-022-04872-1)
63. Bahtiar A, Rahmanita S, Inayatye YD. Pin-hole free perovskite film for solar cells application prepared by controlled two-step spin-coating method. *IOP Conf Ser: Mater Sci Eng*. 2017;196:12037. doi:[10.1088/1757-899X/196/1/012037](https://doi.org/10.1088/1757-899X/196/1/012037)
64. Burschka J, Pellet N, Moon S-J, et al. Sequential deposition as a route to high-performance perovskite-sensitized solar cells. *Nature*. 2013;499(7458):316-319. doi:[10.1038/nature12340](https://doi.org/10.1038/nature12340)
65. Ašmontas S, Čerškus A, Gradauskas J, et al. Impact of cesium concentration on optoelectronic properties of metal halide perovskites. *Materials*. 2022;15(5):1936. doi:[10.3390/ma15051936](https://doi.org/10.3390/ma15051936)
66. Tosado GA, Lin Y-Y, Zheng E, Yu Q. Impact of cesium on the phase and device stability of triple cation Pb-Sn double halide perovskite films and solar cells. *J Mater Chem A*. 2018;6(36):17426-17436. doi:[10.1039/C8TA06391E](https://doi.org/10.1039/C8TA06391E)
67. Choi D-H, Seok H-J, Kim S-K, Kim D-H, Hou B, Kim H-K. The effect of Cs/FA ratio on the long-term stability of mixed cation perovskite solar cells. *Sol RRL*. 2021;5(12):2100660. doi:[10.1002/solr.202100660](https://doi.org/10.1002/solr.202100660)
68. Xu J, Boyd CC, Yu ZJ, et al. Triple-halide wide-band gap perovskites with suppressed phase segregation for efficient tandems. *Science*. 2020;367(6482):1097-1104. doi:[10.1126/science.aaz5074](https://doi.org/10.1126/science.aaz5074)
69. Zhang F, Tu B, Yang S, et al. Buried-interface engineering of conformal 2D/3D perovskite heterojunction for efficient perovskite/silicon tandem solar cells on industrially textured silicon. *Adv Mater (Deerfield Beach, Fla)*. 2023;35(42):e2303139. doi:[10.1002/adma.202303139](https://doi.org/10.1002/adma.202303139)
70. Xu Q, Shi B, Li Y, et al. Diffusible capping layer enabled homogeneous crystallization and component distribution of hybrid sequential deposited perovskite. *Adv Mater (Deerfield Beach, Fla)*. 2023; e2308692. doi:[10.1002/adma.202308692](https://doi.org/10.1002/adma.202308692)
71. Farag A, Fassel P, Hu H, et al. Mitigation of open-circuit voltage losses in perovskite solar cells processed over micrometer-sized-textured Si substrates. *Adv Funct Mater*. 2023;33(3):2210758. doi:[10.1002/adfm.202210758](https://doi.org/10.1002/adfm.202210758)
72. Gharibzadeh S, Fassel P, Hossain IM, et al. Two birds with one stone: dual grain-boundary and interface passivation enables >22% efficient inverted methylammonium-free perovskite solar cells. *Energ Environ Sci*. 2021;14(11):5875-5893. doi:[10.1039/D1EE01508G](https://doi.org/10.1039/D1EE01508G)
73. Saliba M, Correa-Baena J-P, Wolff CM, et al. How to make over 20% efficient perovskite solar cells in regular (n-i-p) and inverted (p-i-n) architectures. *Chem Mater*. 2018;30(13):4193-4201. doi:[10.1021/acs.chemmater.8b00136](https://doi.org/10.1021/acs.chemmater.8b00136)
74. Park B-W, Kedem N, Kulbak M, et al. Understanding how excess lead iodide precursor improves halide perovskite solar cell performance. *Nat Commun*. 2018;9(1):3301. doi:[10.1038/s41467-018-05583-w](https://doi.org/10.1038/s41467-018-05583-w)
75. Liu F, Dong Q, Wong MK, et al. Is excess Pbl 2 beneficial for perovskite solar cell performance? *Adv Energy Mater*. 2016;6(7):1502206. doi:[10.1002/aenm.201502206](https://doi.org/10.1002/aenm.201502206)
76. Kim YC, Jeon NJ, Noh JH, et al. Beneficial effects of Pbl 2 incorporated in organo-lead halide perovskite solar cells. *Adv Energy Mater*. 2016;6(4):1502104. doi:[10.1002/aenm.201502104](https://doi.org/10.1002/aenm.201502104)
77. Tumen-Ulzii G, Qin C, Klotz D, et al. Detrimental effect of unreacted Pbl2 on the long-term stability of perovskite solar cells. *Adv Mater (Deerfield Beach, Fla)*. 2020;32(16):e1905035. doi:[10.1002/adma.201905035](https://doi.org/10.1002/adma.201905035)
78. Meier T, Gujar TP, Schönleber A, et al. Impact of excess Pbl 2 on the structure and the temperature dependent optical properties of methylammonium lead iodide perovskites. *J Mater Chem C*. 2018;6(28):7512-7519. doi:[10.1039/C8TC02237B](https://doi.org/10.1039/C8TC02237B)
79. Song W, Zhang X, Lammar S, et al. Critical role of perovskite film stoichiometry in determining solar cell operational stability: a study on the effects of volatile A-cation additives. *ACS Appl Mater Interfaces*. 2022;14(24):27922-27931. doi:[10.1021/acsami.2c05241](https://doi.org/10.1021/acsami.2c05241)
80. Jesper Jacobsson T, Correa-Baena J-P, Pazoki M, et al. Exploration of the compositional space for mixed lead halogen perovskites for high efficiency solar cells. *Energ Environ Sci*. 2016;9(5):1706-1724. doi:[10.1039/C6EE00030D](https://doi.org/10.1039/C6EE00030D)



81. Fassl P, Lami V, Bausch A, et al. Fractional deviations in precursor stoichiometry dictate the properties, performance and stability of perovskite photovoltaic devices. *Energ Environ Sci*. 2018;11(12):3380-3391. doi:[10.1039/c8ee01136b](https://doi.org/10.1039/c8ee01136b)
82. Fassl P, Zakharko Y, Falk LM, et al. Effect of density of surface defects on photoluminescence properties in MAPbI<sub>3</sub> perovskite films. *J Mater Chem C*. 2019;7(18):5285-5292. doi:[10.1039/C8TC05998E](https://doi.org/10.1039/C8TC05998E)
83. Roose B, Dey K, Chiang Y-H, Friend RH, Stranks SD. Critical assessment of the use of excess lead iodide in lead halide perovskite solar cells. *J Phys Chem Lett*. 2020;11(16):6505-6512. doi:[10.1021/acs.jpcllett.0c01820](https://doi.org/10.1021/acs.jpcllett.0c01820)
84. Khenkin MV, Katz EA, Abate A, et al. Consensus statement for stability assessment and reporting for perovskite photovoltaics based on ISOS procedures. *Nat Energy*. 2020;5(1):35-49. doi:[10.1038/s41560-019-0529-5](https://doi.org/10.1038/s41560-019-0529-5)

## SUPPORTING INFORMATION

Additional supporting information can be found online in the Supporting Information section at the end of this article.

**How to cite this article:** Er-raji O, Bett AJ, Lange S, et al. Toward efficient and industrially compatible fully textured perovskite silicon tandem solar cells: Controlled process parameters for reliable perovskite formation. *Prog Photovolt Res Appl*. 2025;33(1):86-99. doi:[10.1002/ppv.3770](https://doi.org/10.1002/ppv.3770)